Force sensing and transmission in human induced pluripotent stem-cell-derived pericytes

Iendaltseva, O.

Chapter 3

Fibronectin patches as anchoring points for force sensing and transmission in human induced pluripotent stem cell-derived pericytes [1]

abstract

Pericytes (PCs), the mural cells of blood microvessels, have emerged as important regulators of vascular morphogenesis and function. PCs have been reported to participate in the regulation of the capillary diameter and blood flow. Certain pathological conditions such as cerebral ischemia, Alzheimer's disease and diabetic retinopathy are associated with the increase of PC-contractility and overall PC-death. Nevertheless, the degree to which PCs contribute to the regulation of microvessel blood flow is still a matter of controversy. It has been suggested by electron-microscopy that PCs use small deposits of fibronectin (FN), within the laminin (LM) rich basement membrane (BM) aligning the endothelial cells (ECs), as anchoring points to the capillary. Here, we developed an *in vitro* model for PC adhesion plaques and investigated the mechanical aspects of human induced pluripotent stem cell (hiPSC)-derived PCs.

1. This chapter is based on: O. Iendaltseva, V.V. Orlova, C.L. Mummery, E. H. J. Danen and T. Schmidt, Fibronectin Patches as Anchoring Points for Force Sensing and Transmission in Human Induced Pluripotent Stem Cell-Derived Pericytes, published in *Stem Cell Reports*, 2020

Our results showed that PCs strongly prefer FN over LM for the formation of force-loaded adhesion plaques when interacting with a variety of FN/LM patterned substrates. Moreover, we found that PCs sense a preferred FN substrate stiffness in the range of ∼50 kPa on micropillar arrays and ∼25 kPa on continuous substrates. At both lower and higher substrate stiffness, PCs react by dramatically increasing traction force application, altered cytoskeletal organization and cell matrix adhesion distribution patterns in combination with decreased cell spreading behavior. Together, our findings reveal how FN deposits as observed in the BM of microvessels provide anchoring points for mechanical regulation of capillaries by PCs.

3.1 Introduction

Pericytes (PCs) cover the majority of all capillaries in the human body [1]. PCs express markers that are shared with mesenchymal stem cells and smooth muscle cells but, in mid-capillary regions lack smooth muscle actin (SMA) expression [2, 3]. PCs have been shown to promote regulation of vascular development, stabilization and maturation of vessels, and the maintenance of the blood-brain-barrier [4, 5]. Although PCs are essential for the development of the vascular tree [6] their precise role in the control of blood flow through capillaries is still highly debated [7, 8]. PCs are embedded in the capillary basement membrane (BM) and develop characteristic branched processes around microvessels [1, 2]. This morphology together with the presence of contractile proteins like actin, high concentration of myosin, tropomyosin and other [9–12] suggests their functional role in applying mechanical forces to strengthen the blood vessel wall, and their participation in the regulation of microvascular blood flow in particular in the brain [13, 14]. Notably, dysfunction or loss of PCs has been implicated in pathologies such as cerebral ischemia, Alzheimer's disease and diabetic retinopathy [15–18]. Thus, PC-endothelial cell (EC) mechanical interaction represents a potential target for therapy in such conditions.

PCs and ECs build-up a variety of mechanical and biochemical interconnections. They use peg-and-socket contacts that contain gap junctions [19] for direct communication and signaling, cell-to-cell adhesions by N-cadherins [20], and integrin-mediated binding of both cell types to the extracellular matrix of the BM of the capillaries [21]. A critical component of the PC/ECs proper assembly and vessel formation is EphrinB2 reverse signaling. Initial cell-to-cell contact during agiogenesis leads to EphrinB2 engagement by EphB membrane receptors and subsequent EphrinB2 phosphorylation. EphrinB2 phosphorylation, in turn, starts reverse signaling that promotes cell-to-cell adhesion formation [22, 23]. In particular, the integrins and N-cadherins provide two independent adhesion systems that allow PCs to apply forces to their environment and thereby affecting the blood flow in the capillary. It has been shown that PC-EC connections through N-cadherins occur mainly during angiogenesis, being lost with vessel maturation and BM generation [24, 25]. Hence, in mature resting vasculature the mechanical PC-EC connection is dominated by BM-mediated integrin adhesion. The BM in capillaries contains collagen type IV in the outer layer and laminin (LM)-411/511

in the inner layer close to the ECs [26, 27]. PCs are situated within the BM where they may bind collagen and LM. Yet, electron microscopical analysis further suggests a role for $0.2 - 2\ \mu m$ deposits of fibronectin (FN) as specific anchoring points [28–30] (Figure 1.1).

PCs may play an important role in mechanical regulation of the vasculature by providing additional mechanical strength to the endothelium or by regulating blood-flow by their contractility. How this is realized is poorly understood, yet understanding of this process might lead to novel concepts in treatment of pathological conditions, and to the identification of novel targets for therapy. Here we developed an in vitro model to investigate mechanical aspects of PC behavior. We utilized our previously described human induced pluripotent stem cell-derived PCs (hiPSC) with a close to mid-capillary PC phenotype, lacking smooth muscle actin (SMA) expression [31, 32]. Micropatterned surfaces of LM and FN, mimicking BM structures were generated on surfaces varying in mechanical stiffness and in topography. This allowed us to obtain quantitative information on cell morphology and cell contractility. Our results show that (i) PCs strongly prefer FN over LM for adhesion formation, (ii) PCs sense a preferred FN substrate stiffness for spreading, and (iii) PCs respond to either lower or higher stiffness with increased traction forces, altered cytoskeletal organization, and decreased cell spreading. Our results suggest that FN deposits, as observed in the endothelial BM by electron-microscopy, provide the anchoring points for mechanical regulation of capillaries by PCs.

3.2 Methods

3.2.1 Cell culture

CD31– (dif31 and dif43) and SV80 cell lines were cultured in Dulbecco's Modified Eagle's Medium (DMEM, Gibco|Thermo Fisher Scientific, USA) supplemented with 10% fetal bovine serum (HyClone, Etten-Leur, The Netherlands), 25 U/ml penicillin and 25 µg/ml streptomycin (Invitrogen/Fisher Scientific). NIH 3T3 cells were cultured in Dulbecco's Modified Eagle's Medium (DMEM, Sigma) supplemented with 10% calf serum (Thermo Scientific/Sigma), 2 mM glutamine, and 100 µg/ml penicillin/streptomycin. For all experiments cells were seeded at 20 000 cells per sample density directly on the patterned surface. After 4 hours

incubation they were fixed 10' in 4% paraformaldehyde in PBS for immunostaining.

3.2.2 Immunostaining

After cells were fixed, they were permeabilized for 10' with 0.1% Triton-X and blocked for 60' with 1% BSA (Sigma, a2153) in PBS. For cell matrix adhesion assays cells were prepared for staining according to the earlier described method [33]. Briefly, after 4 hours incubation, cells were washed in cytoskeleton buffer (CB), incubated 15" in 0.1-0.25% Triton-X, 0.4% paraformaldehyde and 1µg/mL phalloidin in CB, washed again with CB, and fixed for 10' with 4% paraformaldehyde in CB. In the end they were permeabilized for 10' with 0.5% Triton-X and blocked for 60' with 1% BSA in PBS. Immunostaining was done depending on the experiment, with Alexa532 phalloidin (Thermo Fisher Scientific, a22282), primary antibodies against paxillin (Thermo Fisher Scientific, aho0492), talin (Sigma, t3287), vinculin (Sigma, v9131), alpha-v integrin (Merck Millipore, mab1978), beta-1 integrin (Santa Cruz, sc-18887) and laminin-111 (Sigma, l9393), followed with Alexa532/647 conjugated secondary antibody against mouse IgG (Thermo Fisher Scientific, a11002/Jackson, 115-605-006 respectively) and Alexa647 conjugated secondary antibody against rabbit IgG (Thermo Fisher Scientific, a21244).

3.2.3 PDMS surface patterning with FN and LM

PDMS surface with a pattern, where LM would surround FN spots or inverse, was produced by combining "stamp-off" and "microcontact printing" methods [34]. Two flat PDMS (Sylgard 184,Dow Corning) 1:30 (crosslinker:prepolymer ratio, cured 16 hours at 65°C) stamps were separately incubated for 60' with a 40 µl drop of 50 µg/ml LM-111 (Sigma, l2020) in milliQ water and a 40 µl mixture of 50 µg/ml FN (Sigma, f1141) plus 10 µg/ml Alexa405-FN in milliQ, washed with milliQ and dried under laminar flow. With a help of UV-ozone activated PDMS 1:10 micropillar arrays, where 2 µm diameter pillars with 2 µm spacing and hexagonal order, were obtained holes in one of the layers. Further, two stamps were inverted one by one on top of the UV-ozone activated PDMS 1:10 surface and incubated for 10' each, to get previously modified protein sheet on top of the uninterrupted layer of the second (Fig. 2.2a, b).

PDMS surfaces with a grid of crossing FN and LM lines were obtained in a similar manner. First, two PDMS 1:10 molds with 5 μm high lines of different width were produced by using replica-molding from a silicon wafer. After UV-ozone activation 10', they were pushed onto PDMS 1:30 stamps with a protein layer dried on them. Followed by 10' incubation and removal, this molds left a negative of the pattern in the protein layer on top of the PDMS stamps. Further, PDMS stamps were inverted on top of the UV-ozone activated PDMS 1:10 surface, creating a pattern of crossing LM and FN lines on it (Fig. 2.3a).

PDMS surfaces with FN lines under a layer of LM with holes were printed by using PDMS stamps with LM and FN layers modified as aforementioned. PDMS micropillar array was used to make holes in the dry LM monolayer and PDMS mold with lines – to create a line pattern in FN. Further, this stamps were loaded on top of the UV-ozone activated PDMS surface, with FN stamp going first (Fig. 2.3b). Finally, all patterned PDMS surfaces were blocked by using 1% BSA 60'.

3.2.4 PDMS micropillar array preparation

PDMS micropillar arrays were prepared as was described before [35, 36]. Briefly, SI mold was made by two-step Deep Reactive Ion Etching (DRIE) process. This yielded a 10×10 mm hexagonal array of 2 μm diameter holes with 2 μm spacing and varying depth, flanked by two 50 μm deep 10×2 mm tranches. After mold passivation with trichloro silane (Sigma), PDMS 1:10 was poured over it and cured for 20 hours at 110°C. The peeled off PDMS had a negative of the mold shape with micropillar array and 50 μm high spacers on the sides of it. This array was functionalized with the help of PDMS 1:30 stamps and dried protein of interest on top of them. A 40 μl drop of FN or LM-111 mixture in water was incubated for 60' on the PDMS 1:30 stamp, then washed and dried under laminar flow. This stamp was then genly loaded onto UV-ozone activated PDMS micropillar array for 10'. Finally, stamped array was blocked with 0.2% Pluronic (F-127, Sigma) in PBS for 60' at room temperature and washed with PBS.

3.2.5 Hydroxy-PAAm gel preparation

Hydroxy-PAAm hydrogels were made following a previously described method [37]. Gels stiffer then 40 kPa were obtained following the same

procedure as suggested in [38] and [39] by increasing polyacrylamide monomer concentration with a fixed monomer/crosslinker ratio of 29:1. Further gels were stamped with LM&FN pattern where FN spots were surrounded by LM. This was achieved by using an adapted "stamp-off" and "micro-contact printing" approaches described in [34]. A 40 µl drop of 50 µg/ml LM-111 in milliQ water was incubated for 60' on top of the 10×10 mm PDMS 1:30 stamp, followed by washing and drying under laminar flow. Then OV-ozone activated PDMS micropillar array was pushed onto the dry LM-111 monolayer to obtain holes in the places of micropillar-LM-111 contacts. After 10' incubation the array was removed and a second 40 µl drop of 50 µg/ml FN plus 10 µg/ml Alexa405-FN in milliQ was gently spread onto the first layer for 60'. Finally, the stamp was washed and dried under laminar flow. Hydroxy-PAAm hydrogels were dried using nitrogen flow and incubated with the stamp for 60' (Fig. 2.6a), following blocking with 1% BSA in PBS o/n and washing with PBS.

3.2.6 Microscopy

Confocal imaging was performed on a home-built setup based on an Axiovert200 microscope body (Zeiss), spinning disk unit (CSU-X1, Yokogawa) and an emCCD camera (iXon 897, Andor). IQ-software enabled setup-control and data acquisition. Lasers of 405 nm (CrystaLaser), 488 nm (Coherent), 514 nm, 561 nm (Cobolt) and 642 nm (Spectra Physics) wavelength were coupled into the CSU via polarization maintaining single-mode fiber. Spacers on the sides of micropillar arrays allowed placing them upside down onto #0 coverslips (Menzel Glaser) with adhered cells facing down. This approach ensured reproducible cell observation within the limited working distance of a high-NA objective on an inverted microscope. For PDMS and hPAA 2D assays parafilm spacers were made directly on top of the glass coverslips.

3.2.7 Image analysis

Cell spreading area was quantified by using FIJI software. First the background was subtracted by adjusting threshold level, followed by the cell edge selection with a tracing tool. In the end the mean values for at least 30 cells per condition were calculated.

Cell traction forces were measured by using micropillar array technology [36, 40, 41] and quantified as previously described [35]. Micropillar tops were functionalized with fluorescently labeled FN or LM with further immunostaining. This allowed us to detect deflections with ∼30 nm accuracy that corresponded to 500 pN for soft and 2 nN for stiff pillars force precision by using a specifically designed Matlab script.

Cell-matrix adhesion area was determined as mentioned in [42]. Fluorescent images of cell-matrix adhesion proteins were passed through a Gaussian low pass filter, then – hole-filling algorithm and watershed segmentation. In the end all results were manually controlled to remove images with incorrect adhesion detection due to a low signal-to-noise ratio.

3.2.8 Statistical analysis

To assess significance of the difference between two conditions, the Wilcoxon rank sum test in the Matlab program was used. This test is an equivalent to a Mann-Whitney U test. Significance for the force application by PCs represented in the graph 3.3e was quantified by using ANOVA test comparing means of the mean values determined for at least three independent experiments per each stiffness.

3.3 Results

3.3.1 Preferred binding of PCs to FN patches on multilayered substrates.

We investigated whether PCs may preferentially use FN deposits for attachment onto capillaries. As a source for PCs, we used hiPSC line LUMC06iCTRL-derived PCs [32, 43]. As hallmarks for PCs, these cells lacked the endothelial marker CD31, they expressed the PC/mesenchymal stem cell markers PDGFRβ, NG2, CD146, CD44, CD73, CD105, they expressed very little to no smooth muscle actin (SMA), very little SMC markers such as (SM)22 and Calponin (CNN1), all distinguishing them from SMCs. Moreover, as we described earlier, these PCs promote vascular development in PC-EC co-cultures [31, 32].

We modeled LM and FN arrangements in the endothelium-PC interstitia, which has been described by electron microscopy previously [28]. In EM-studies it was shown that FN was arranged in the form

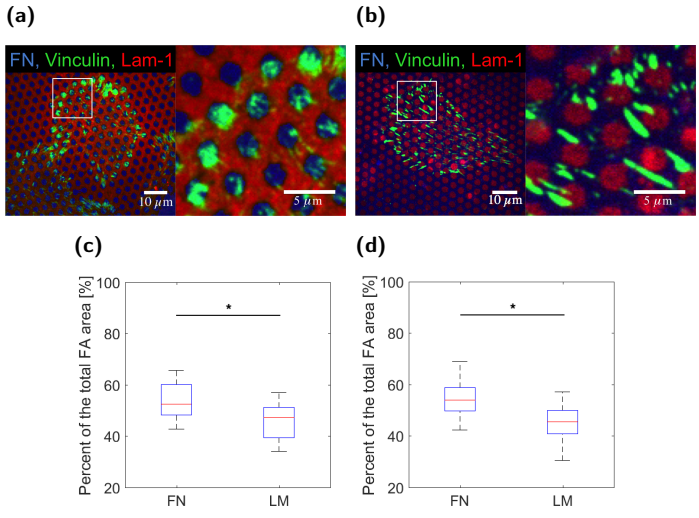

Figure 3.1: PCs placed on PDMS flat surfaces stamped with FN&LM-111. (a) Confocal immunofluorescence images of PCs (dif31) seeded on the type of pattern depicted in (2.2a) with vinculin labeled (green). Confocal immunofluorescence images of PCs (dif31) seeded on the type of pattern depicted in (2.2b) with vinculin labeled (green). (c) Percentage of PC (dif31) focal adhesions (FAs) located on FN and LM for (a). (d) Percentage of PC (dif31) focal adhesions (FAs) located on FN and LM for (b). (c) and (d) results are derived from three independent experiments performed in minimum two replicates. At least 10 images were analyzed from each sample. NS, P>0.05; *P<0.05; **P<0.005; ***P<0.0005 according to Mann - Whitney test. See also Figure 3.8.

of micrometer-sized patches surrounded by LM-411/511 within the BM of capillaries (Figure 1.1). To mimic the *in vivo* observations in our *in vitro* experiments we used a multilayer stamp-off method [34] (Figure 2.2). First, a PDMS micropillar array consisting of 2 μm wide pillars in a hexagonal arrangement of 2 μm spacing, activated in an UV-ozone cleaner was pressed onto and released from a LM monolayer deposited on a flat PDMS substrate. The procedure left a homogeneous LM layer with patterned holes on the flat PDMS stamp. Subsequently, this layer was transferred onto a second flat FN-coated PDMS surface. In the resulting multilayered surface, FN was accessible through the holes in the LM layer (Figure 2.2a). For visualization FN was mixed with a low amount (<1%) of Alexa-405 conjugated FN. LM-111 was visualized using an anti-LM-

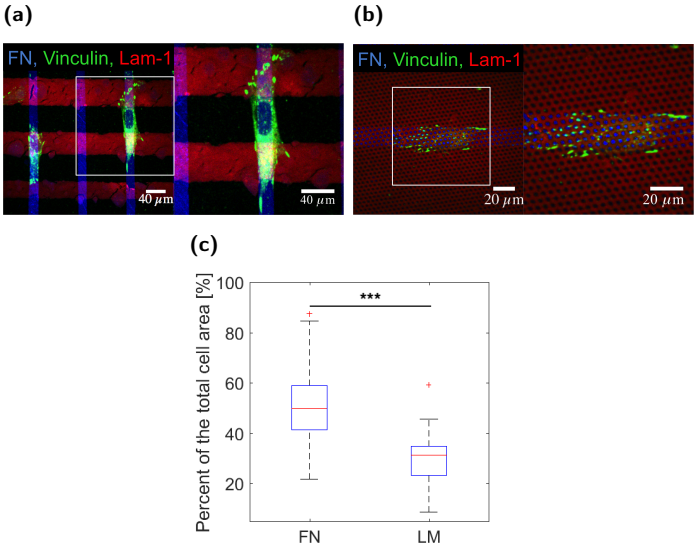

Figure 3.2: PCs placed on PDMS flat surfaces stamped with FN&LM-111. (a) Confocal immunofluorescence images of PCs (dif31) seeded on the type of pattern depicted in (2.3a) with vinculin labeled (green). (b) Confocal immunofluorescence images of PCs (dif31) seeded on the type of pattern depicted in (2.3b) with vinculin labeled (green). (c) Percentage of PC (dif31) focal adhesions (FAs) located on FN and LM for (a). In (c), the results are derived from three independent experiments performed in minimum two replicates. At least 10 images were analyzed from each sample. NS, $P>0.05$; *$P<0.05$; **$P<0.005$; ***$P<0.0005$ according to Mann - Whitney test

111 antibody followed by staining with an Alexa-647-coupled secondary antibody.

PCs were incubated for 4 hours on the patterned substrates, fixed, and stained for F-actin and cell-matrix adhesion proteins. PCs could readily attach and spread on substrates coated with either LM or FN monolayers. However, in the patterned combined protein model, cells strongly preferred to attach to FN patches and avoided areas covered by LM. Vinculin and α_v-integrin staining showed cell-matrix adhesions formed preferentially on FN patches, avoiding areas containing LM (Figure 3.1a, c, 3.8a).

To rule-out effects caused by the order in which FN and LM were stamped on the surface, an inverse approach was taken. First the stamp-off method was used to create holes in the FN monolayer, which was sub-

sequently transferred onto a flat PDMS surface coated with LM (Figure 2.2b). Again, vinculin staining revealed that PCs formed cell-matrix adhesions almost exclusively on the FN-coated area whereas LM-111-coated areas were avoided (Figure 3.1b,d).

We further generated substrates consisting of crossing stripes of LM and FN by stamping a PDMS surface with a grid of $20-60$ μm LM-111 and 20 μm FN lines (Figure 2.3a). Cells aligned on top of the FN-lines and avoided areas, which were stamped by LM. Vinculin staining showed that PCs developed cell-matrix contacts mainly on the vertical FN stripes, but not with the horizontal LM lines (Figure 3.2a, c). Finally, we combined the two micro-structuring techniques and generated surfaces in which 20 μm FN lines were placed under a layer of LM into which 2 μm diameter holes were incorporated (Figure 2.3b). Strikingly, PCs were able to sense the small regions where FN was exposed through the holes in the LM layer, localized adhesions at these spots, and fully aligned to the FN stripes (Figure 3.2b).

Together, our data showed that PCs adhered preferentially to FN, while avoiding LM areas when FN was present. This suggests that FN deposits in the PC-EC interstitia in capillaries, as previously identified by electron microscopy [28–30], may indeed serve as preferred points for PC attachment to capillaries in the capillary BM.

3.3.2 Highest PC spreading is accompanied by lowest force application on FN substrates of intermediate stiffness.

Next, we investigated whether FN deposits serve as mechanical anchoring points where PCs can sense and respond to variations in mechanical properties of capillaries and, *vice versa*, apply forces to mechanically modulate the extracellular matrix. As a model, PDMS micropillar arrays were generated using the same geometry as described above (Figure 3.3a). By varying the height of the pillars between $3-7$ μm the effective stiffness of the arrays was 11.6, 29.5, 47.2, and 137 kPa, respectively (Figure 3.3b). This range of stiffness resembles that reported for a variety of tissues [44, 45]. The pillar tops were functionalized with FN to which a low amount ($< 1\%$) of Alexa 405/647-labeled FN was added. Such fluorescence labeling allowed monitoring pillar deflections and calculation of cellular traction forces to an accuracy of 0.5 nN using a fluorescence microscope (Figure 3.3c) [35].

3.3 Results

(a)

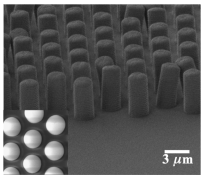

(b)

Stiffness (kPa)	Height (μm)	Diameter (μm)
11.6	6.9	2
29.5	6.1	2.1
47.2	4.1	1.9
137	3.2	2

(c)

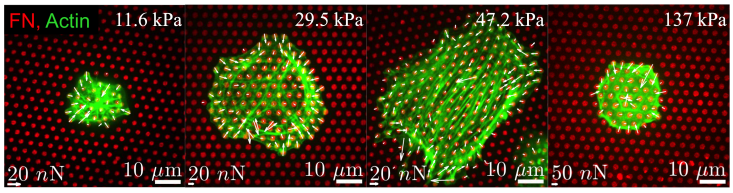

(d)

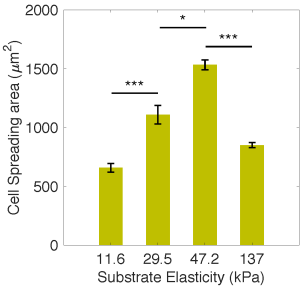

(e)

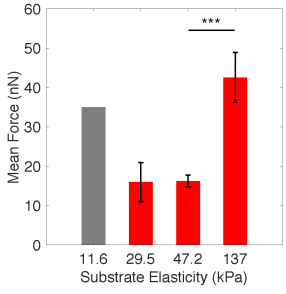

(f)

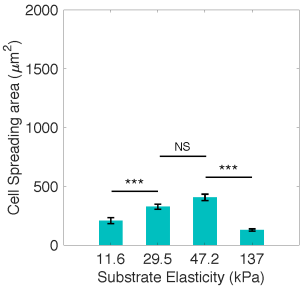

(g)

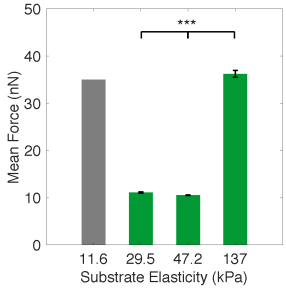

Figure 3.3: PCs placed on PDMS micropillar arrays of different stiffness stamped with FN. (a) An example SEM image of the micropillar array. (b) A table with pillar dimensions per stiffness used for experiments (c) Confocal immunofluorescence images showing PCs (dif31) (actin staining in green) seeded on PDMS micropillar arrays of four different stiffness (from left to right: 11.6, 29.5, 47.2, 137 kPa), functionalized with FN (red). Forces exerted on pillars are depicted with white arrows. (d, f) Average cell spreading area for two different PC lines (d PC dif31, f PC dif43) on PDMS micropillar arrays after 4 hours incubation. (e, g) Average force application for two different PC lines (e PC dif31, g PC dif43) measured after 4 hours incubation on PDMS micropillar arrays. Note that on 11.6 kPa micropillar arrays $\sim$ 25% pillars collapsed due to the apparent high forces, precluding deflection analysis. The gray bar represents the minimal force necessary for the pillar deflection equal to the interpillar distance. Actual average force may be higher. All error bars are s.e.m. derived from five for PC dif31 line and three for PC dif43 line independent experiments performed in minimum two replicates. At least 30 cells were analyzed from each sample. NS, $P>0.05$; *$P<0.05$; **$P<0.005$; ***$P<0.0005$ according to Mann - Whitney test (d, f, g) or ANOVA for (e). See also Figure 3.9.

PCs derived from two independent differentiations (dif31 and dif43) were seeded onto the pillar arrays, fixed after 4 hours and stained for F-actin. Previously we showed that fixation had negligible effect on the analysis of cell spreading and force measurements [42]. PC spreading and force exertion varied with variations in substrate stiffness between 12-137 kPa. Spreading was highest at an intermediate substrate stiffness between 30-47 kPa, resulting in a mean cell area of up to 1500 μm^2, for one PC (dif31) line and $\sim$ 500 μm^2 for another PC (dif43) line. Spreading significantly decreased at both lower and higher substrate stiffness to below 800 μm^2 for PC (dif31) line and $\sim$ 200 μm^2 for PC (dif43) line (Figure 3.3d f). The optimal spreading on intermediate substrate stiffness was paralleled by a low cellular force generation of 10 – 15 nN/pillar for both PC lines (Figure 3.3e,g). On pillars of either lower or higher stiffness, the decrease in spreading was accompanied by significantly higher force generation, reaching 35 – 40 nN/pillar for both PC lines (note: the high mean force value at the lowest substrate stiffness of 11.6 kPa refers to a lower limit since $\sim$ 25% of the pillars collapsed onto each other due to excessive forces under these conditions and could not be analyzed).

This behavior was different from the behavior of fibroblasts. For both SV80 (Figure 3.9a,3.9b) and NIH-3T3 (Figure 3.9c,3.9d) cellular forces gradually increased with substrate stiffness, in line with previous reports

[46, 47]. Across this stiffness range, spreading was largely constant for both fibroblast lines.

We further analyzed how variations in substrate stiffness affected formation and properties of cell-matrix adhesions. Immunofluorescence staining was applied to detect the focal-adhesion proteins vinculin, paxillin and talin on top of the micropillars. As reported earlier, focal-adhesions developed solely on pillars at which cells applied a force [35]. The average cell-matrix adhesion area was determined (Figure 3.4). Remarkably, for all components analyzed the cell matrix adhesion area decreased from $\sim 2\ \mu m^2$ at intermediate stiffness substrates to $< 1.5\ \mu m^2$ at high stiffness substrates (Figure 3.4g). Surprisingly, the correlations between size of the cell-matrix adhesion, the applied cellular force, and the substrate stiffness, as reported for various fibroblast cell lines [35, 48, 49], did not hold for the hiPSC-derived PCs studied here.

Together our findings suggest that PCs bind specifically to FN-patches and sense and respond to changes in stiffness between 12 – 137 kPa. In contrast to fibroblasts for which we observed a continued increase in traction force with increasing substrate stiffness, PCs suppress traction forces and increase cell spreading within 30 – 50 kPa matrix stiffness range, while applying strong traction forces accompanied by limited cell spreading on both soft and stiff substrates.

3.3.3 A switch in PC cytoskeletal organization on stiff substrates.

To further examine what may underlie the increased force application at reduced focal-adhesion area on stiff micropillars, we analyzed the organization of the F-actin cytoskeleton (Figure 3.5a). F-actin was labeled by phalloidin and the 3D-structure of the actin skeleton was imaged for the various substrate stiffness. While straight, elongated F-actin stress fibers were visible on pillars of intermediate stiffness, on stiff micropillars PCs appeared to engulf the pillars and form ring-like F-actin structures that embraced multiple pillars. Notably, all array surfaces, excluding the upper pillar surface, were thoroughly passivated by Pluronic effectively preventing cell attachment. Indeed, the F-actin rings observed below the upper surface of stiff pillars were not supported by cell-matrix adhesions. A 3D-analysis of the location of the different components showed

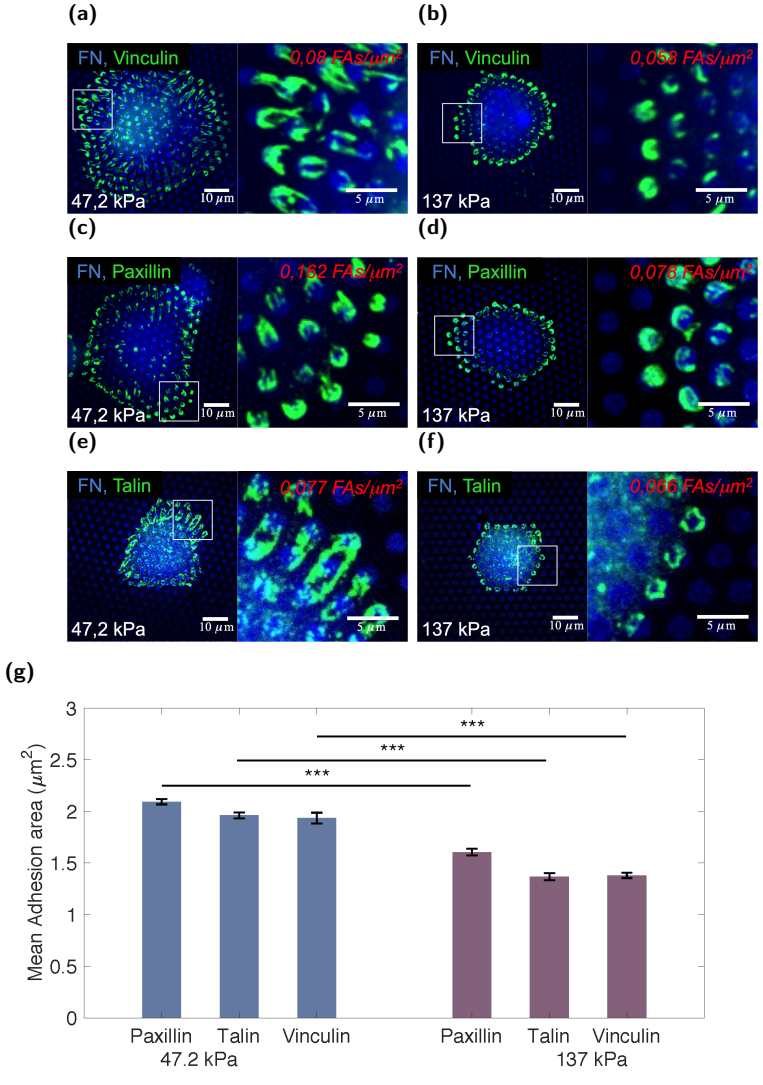
(a)
(b)
FN, Vinculin
0,08 FAs/μm²
47,2 kPa
FN, Vinculin
0,058 FAs/μm²
137 kPa
10 μm
5 μm
(c)
(d)
FN, Paxillin
0,162 FAs/μm²
47,2 kPa
FN, Paxillin
0,074 FAs/μm²
137 kPa
(e)
(f)
FN, Talin
0,077 FAs/μm²
47,2 kPa
FN, Talin
0,060 FAs/μm²
137 kPa
(g)
Mean Adhesion area (μm²)
***
Paxillin
Talin
Vinculin
47.2 kPa
137 kPa

Figure 3.4: Cell matrix adhesion area of PCs (dif31) placed on PDMS micropillar arrays of high (137 kPa) and intermediate (47.2kPa) stiffness. (a – f) Confocal immunofluorescence images of PC (dif31) seeded on PDMS micropillar arrays of two different stiffness (137 kPa and 47.2 kPa), functionalized with FN (blue). Cells were stained for vinculin (a,b), paxillin (c,d) and talin (e, f) (green). (g) Average cell matrix adhesion area of PCs cells on PDMS micropillar arrays with 137 kPa stiffness (right) and – 47.2 kPa (left), after 4 hours incubation. All error bars are s.e.m. derived from two independent experiments performed in minimum two replicates. At least 30 cells were analyzed from each sample. NS, $P>0.05$; *$P<0.05$; **$P<0.005$; ***$P<0.0005$ according to Mann - Whitney test. See also Figure 3.10.

that on stiff pillar arrays actin fibers (green) were $\sim 1.5\ \mu m$ below the FN-coated (blue) pillar tops whereas cell matrix adhesion components (vinculin, red) were exclusively localized at the upper surface (Figure 3.5a). By contrast, on pillar arrays of intermediate stiffness, FN, vinculin and F-actin all coincided within $0.8\ \mu m$ at the upper pillar surface.

To analyze the role of cytoskeletal tension and cellular traction force application in relation to the switch in cytoskeletal organization on stiff substrates, PCs were treated with a low concentration ($0.5\ \mu M$) of the ROCK inhibitor Y-27632. ROCK inhibition led to an increased spreading area of PCs on soft as well as stiff substrates, while the cell area on pillars of intermediate stiffness was hardly affected (Figure 3.6a). This indicated that the spreading area was limited by strong cellular contractile forces on soft and stiff substrates. Indeed, traction forces on stiff micropillars, but not on pillars of intermediate stiffness were suppressed by a factor of ~ 1.2 in the presence of Y-27632 (Figure 3.6b). Moreover, the reduction of traction forces caused by ROCK inhibition was accompanied by loss of the ring-like structures surrounding pillars (Figure 3.6c) and reversal of PC cytoskeletal morphology to parallel F-actin stress fibers located on top of the pillar arrays (Figure 3.6d).

3.3.4 Suppression of PC spreading on 2D patterned FN substrates of high and low stiffness

We next investigated whether the switch in cytoskeletal organization and the suppression of cell spreading on stiff micropillars was determined by the 3D topography of the micropillar arrays. For this purpose, 2D micropatterned substrates were designed, which consisted of FN spots within a LM monolayer on a flat surface whose stiffness could be var-

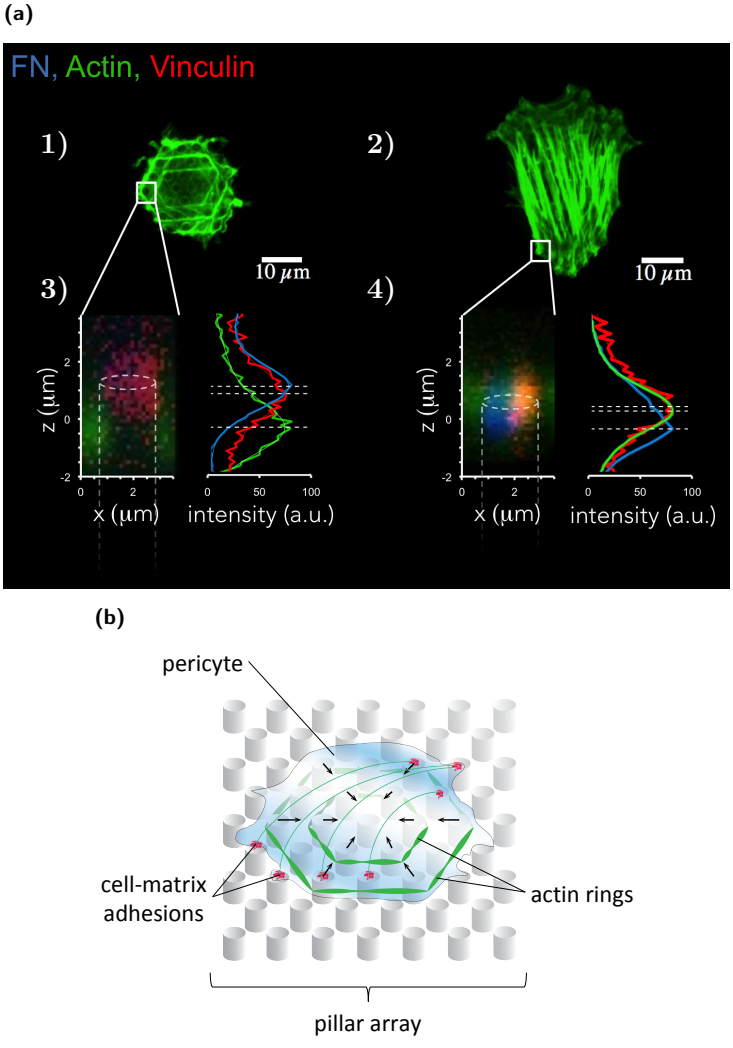

Figure 3.5: Differential actin cytoskeleton organization of PCs. (a) Confocal images of the PCs (dif31) actin cytoskeleton organization on 1) 137 kPa and 2) 47.2 kPa pillars. (a) 3) and 4) on the left – z-projections of the boxed area showing actin (green) and vinculin (red) localization relatively to FN (blue) coated micropillars; on the right – intensity profiles of the z – projections, normalized to 100. (b) Schematic representation of the PCs actin cytoskeleton organization on stiff micropillars. See also Figure 3.11.

(a)

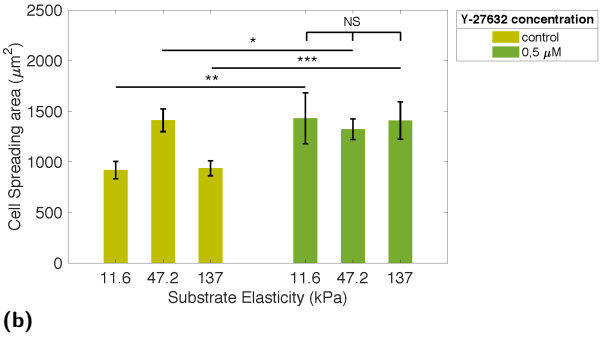
Cell Spreading area (μm^2)
2500
2000
1500
1000
500
0
NS
*
***
**
11.6
47.2
137
11.6
47.2
137
Substrate Elasticity (kPa)
Y-27632 concentration
control
0,5 μM

(b)

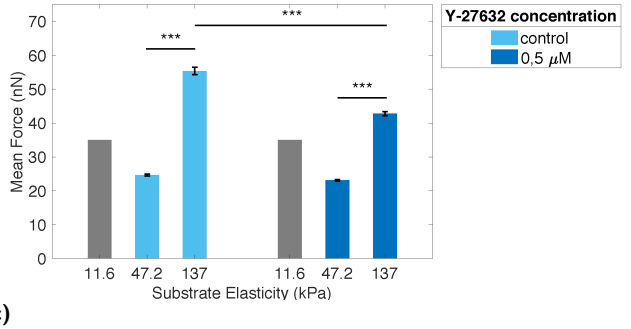
Mean Force (nN)
70
60
50
40
30
20
10
0
***
***
***
11.6
47.2
137
11.6
47.2
137
Substrate Elasticity (kPa)
Y-27632 concentration
control
0,5 μM

(c)

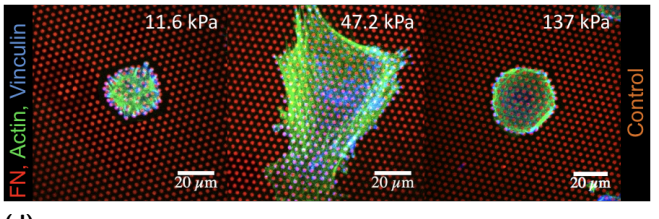
FN, Actin, Vinculin
11.6 kPa
47.2 kPa
137 kPa
Control
20 μm
20 μm
20 μm

(d)

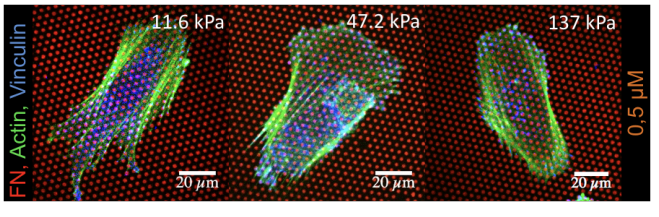
FN, Actin, Vinculin
11.6 kPa
47.2 kPa
137 kPa
0,5 µM
20 μm
20 μm
20 μm

Figure 3.6: Inhibition of ROCK alters PCs spreading on stiff (137 kPa) and soft (11.6 kPa) PDMS micropillar arrays. (a) Average PCs (dif31) spreading area without (left) and with (right) Y-27632 (0.5 μM) after 4 hours incubation. (b) Average PCs (dif31) forces respectively. (c – d) Representative immunofluorescence images of PCs (dif31) spreading and actin cytoskeleton organization (green) on PDMS micropillars (red) without Y-27632 (c) and with 0.5 μM Y-27632 (d) after 4 hours incubation. All error bars are s.e.m. derived from two independent experiments performed in minimum two replicates. At least 30 cells were analyzed from each sample. NS, $P>0.05$; *$P<0.05$; **$P<0.005$; ***$P<0.0005$ according to Mann - Whitney test.

ied, ranging from 3.6 kPa to 250 kPa. As surface we utilized hPAAm hydrogels that provide the same flexibility in substrate micropatterning as PDMS gels, but allow more precise stiffness modulation [37]. Flat PDMS stamps were generated and coated with a layer of LM-111 containing a hexagonal pattern of 2 μm-wide holes of 2 μm spacing, which was covered by a FN monolayer, creating a double layer of LM and FN. This stamp was subsequently inverted onto the hPAAm hydrogels of varying stiffness to print a pattern of FN spots embedded in LM similar to the geometry described in Figure 2.2a (Figure 3.7a). The stiffness of the hPAAm substrate was varied between 3.6 – 250 kPa, a stiffness range within what has been described for blood vessels [50–53].

PCs were seeded onto these flat micropatterned substrates and fixed after 4 hours of incubation. As observed for the pillar arrays the spreading area followed a bell-shaped curve with low spreading at low and high stiffness, and increased spreading at intermediate stiffness. The spreading area doubled to its maximum value at 25 kPa (1200 ± 60 μm^2 on 3.6 kPa *vs* 2500 ± 120 μm^2 on 25 kPa), and decreased at high stiffness (1600 ± 80 μm^2 on 40 kPa) (Figure 3.7c). The cell spreading area on micropatterned hPAAm gels up to 250 kPa was still significantly lower than that observed on a continuous substrate of non-physiological stiffness such as PDMS (1 MPa) and glass (1 GPa) (Figure 3.7d). The preference of PCs to attach to FN over LM was again seen on micropatterned hPAAm substrates. Areas covered with LM were less distorted than areas covered with FN indicating a preferential force application on FN-covered areas (Figure 3.7b). Furthermore, on gels with a stiffness >40kPa, the extracellular matrix coating was disrupted from the surface, further indicating the high forces applied by PCs at high substrate stiffness (Figure 3.7b).

3.3 Results

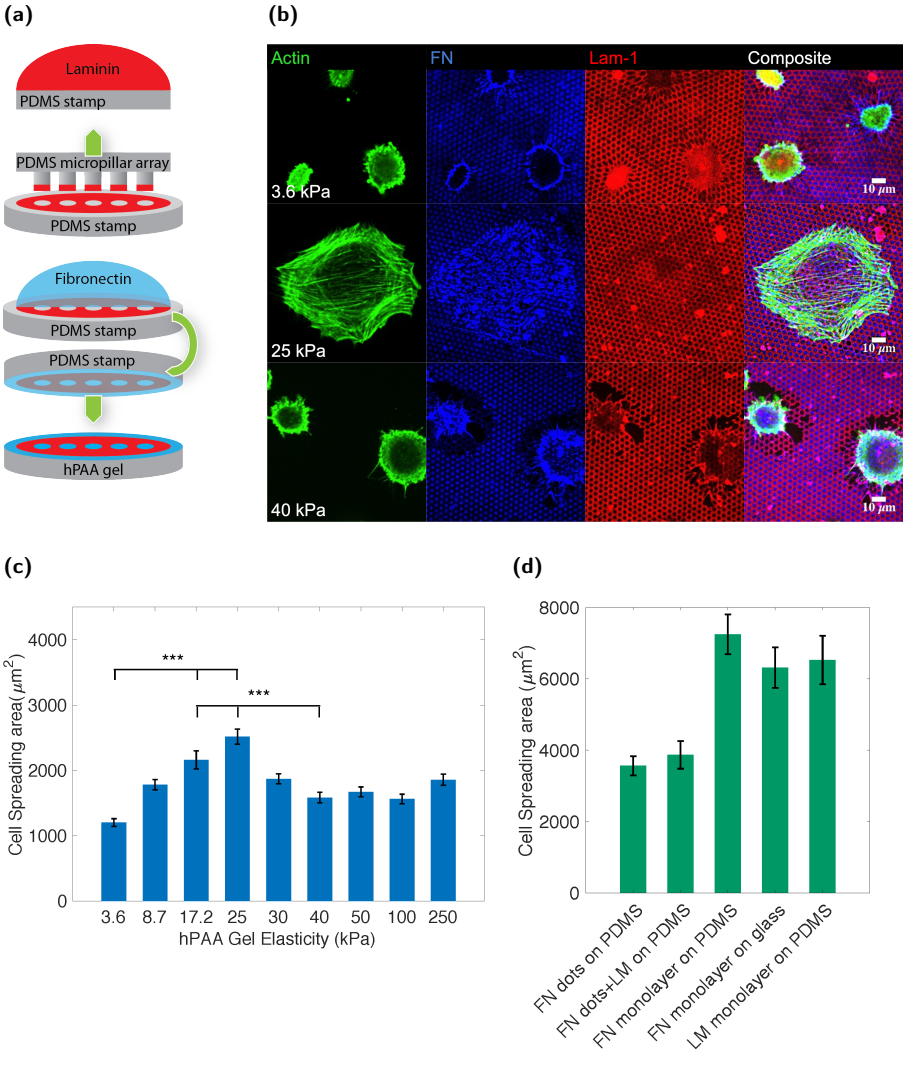
(a)
Laminin
PDMS stamp
PDMS micropillar array
PDMS stamp
Fibronectin
PDMS stamp
PDMS stamp
hPAA gel
(b)
Actin
FN
Lam-1
Composite
3.6 kPa
25 kPa
40 kPa
10 μm
(c)
Cell Spreading area(μm²)
4000
3000
2000
1000
0
***
***
3.6 8.7 17.2 25 30 40 50 100 250
hPAA Gel Elasticity (kPa)
(d)
Cell Spreading area (μm²)
8000
6000
4000
2000
0
FN dots on PDMS
FN dots+LM on PDMS
FN monolayer on PDMS
FN monolayer on glass
LM monolayer on PDMS

Figure 3.7: PCs (dif31) spreading on hydroxy-PAAm hydrogels of different stiffness. (a) "micro contact printing" scheme of hPAAm hydrogels with FN spots surrounded by LM-111. (b) Representative immunofluorescence images of PCs (dif31) seeded on hydroxy-PAAm hydrogels of 3.6, 25 and 40 kPa stiffness (from top to bottom) (c) Average PCs (dif31) spreading area on a palette of hydroxy-PAAm hydrogels with different stiffness and FN&LM stamping. (d) PCs (dif31) spreading on PDMS flat surfaces stamped with: 1) FN dots, 2) FN dots surrounded by LM-111, 3) FN monolayer, 4) LM-111 monolayer; and glass coated with FN monolayer. All surfaces were blocked with BSA 1%. All error bars are s.e.m. derived from three independent experiments performed in minimum two replicates. At least 30 cells were analyzed from each sample. NS, $P>0.05$; *$P<0.05$; **$P<0.005$; ***$P<0.0005$ according to Mann - Whitney test.

3.4 Discussion

PCs have been implicated in regulation of microvessel blood flow and capillary diameter in health and disease. Thus, the mechanical PC-endothelium interaction represents a potential target for therapy. However, it is not understood whether PCs actively and directly participate in control of the vascular diameter, nor is it understood how a putative mechanical connection between PCs and ECs is regulated. N-cadherin mediated binding of PCs to ECs is important during angiogenesis [6], yet N-cadherin expression by ECs is down-regulated with vessel maturation and BM formation [24, 25]. Therefore, adhesion to the BM represents the most likely connection between PCs and ECs in mature, resting capillaries. The BM has a complex composition. Earlier studies pointed to a particular role for small FN-deposits embedded in the LM-rich BM for PC adhesion [28].

Our results support the role of FN deposits in PC interaction with the BM. By modeling FN deposits and their mechanical properties in different ways, we show that PCs have a strong preference towards FN over LM. PCs organize their cell-matrix adhesions mainly on FN while avoiding LM. PCs are guided by thin stripes of FN dots embedded in a LM layer. Interestingly, in the BM of tumor capillaries, FN is frequently over-expressed and is not organized as small distributed patches, but as a thick homogeneous layer [54]. This has been shown to be accompanied by a loose association between PCs and ECs, the opening of spaces separating the two cell types, and the formation of long PC protrusions into the tumor parenchyma, all resulting in wide, leaky microvessels

[55]. Similar effects were reported in the complete absence of FN [21]. Nevertheless, PCs can also leave ECs in injury or normal development conditions and act as progenitor/stem cells [30, 56–58]. Notably, in PC-EC co-cultures, FN expression was found up-regulated in ECs, yet down-regulated in PCs [21], implying that FN in the capillary BM originates mainly from ECs. Hence, it is conceivable that a tight cross talk between ECs and PCs exists, which orchestrates the formation of a LM-rich BM containing small FN deposits. Altogether, our work and the previous findings point to a critical role for the organization of FN deposits in the LM-rich BM for PC adhesion and microvascular function.

Our data provide evidence that capillary FN deposits can serve as points for PC mechanosensing and mechanotransduction. PCs respond to the variation in FN-patterned substrate stiffness with changes in force application, spreading, and cell-matrix adhesions size. PCs show optimal spreading on intermediate (20 – 40 kPa) substrate stiffness, whereas the spreading area was suppressed on both soft and stiff, which is paralleled by an increased size of cell-matrix adhesions on intermediate stiffness substrates. Such mechanoresponsive behavior aligns with the "molecular-clutch hypothesis" [59], which assumes that a response to mechanical cues decreases below or above an optimal rigidity by an increase in the molecular unbinding rate. The increased unbinding would result in lower cell forces, smaller cell substrate adhesions and an ineffective cell spreading on very soft and very rigid matrices. The molecular-clutch model faithfully describes the mechanoresponse of neuronal growth-cones and glioma cells [59–61]. Remarkably, we find that forces applied by PCs on intermediate stiffness substrates are lower than on soft or stiff substrates, which differs from earlier observations with other, in particular fibroblastic, cell types [62][63]. Our own direct comparison with human and mouse fibroblasts where cellular traction forces gradually increase with increasing substrate stiffness corroborate those findings. Another prediction of the molecular-clutch model is the cellular response to suppression of myosin activity [59]. Indeed, we observe that mild ROCK inhibition, which would attenuate force generation, improves PC spreading on stiff and soft substrates.

The high forces and small spreading area observed for PCs on stiff micropillar arrays were accompanied by a dramatic change in cytoskeletal F-actin organization. In comparison to the linear organization of stress fibers on intermediate stiffness pillars, PCs formed circular F-actin rings

surrounding very stiff micropillar arrays. Cell-matrix adhesions assembled on the FN-coated surface of such pillar arrays, but the actin-ring structures encircled multiple pillars below the pillar tops. We hypothesize that such engulfing through ring-like F-actin cytoskeleton organization could represent a cell adaptation process towards the "frictional slippage" regime earlier described [64], allowing PCs to increase forces on substrates outside their optimal rigidity. In line with this hypothesis, we found that mild ROCK inhibition reversed the change in F-actin cytoskeletal organization back to an organization as observed on intermediate stiffness.

The use of flat hPAAm hydrogels instead of PDMS micropillars, allowed us to eliminate the effect of substrate topography while keeping the opportunity to tune the substrate stiffness. On flat 2D micropatterned surfaces the PC behavior was similar to that found on micropillar arrays: PCs showed optimal spreading on intermediate stiffness substrates. Yet, we noticed that the optimal stiffness for PC spreading differed on hPAAm hydrogels (25 kPa) to that on PDMS micropillar arrays (47 kPa). This small, yet significant, difference is likely due to the 2D versus 3D geometry of the substrates, the tightly restricted area for cell-matrix adhesions on the micropillar arrays, and/or the absence of LM in the micropillar model system. Interestingly, for micropatterned hydrogel substrates, the stiffness range of 15 – 25 kPa supporting optimal PC spreading was close to that determined by atomic-force microscopy for ECs and smooth muscle cells [44, 45], indicating that this stiffness range represents a response in a physiologically relevant stiffness regime. Behavior of PCs observed in this study may provide an insight on the way PCs distinguish deviations of the microvessel stiffness from the normal and react by increasing contractile forces. A limitation of this study is the unavailability of *ex vivo* isolated mid-capillary PCs. We derived CD31– PCs from a hiPSC line and used different differentiations. Robustness of PC behavior described here could be further increased using PCs derived from multiple independent hiPSC lines in future studies.

Taken together, our study shows that PCs strongly prefer FN over LM, that PCs recognize and align to FN dots within a LM substrate, that PCs apply forces to FN deposits, and that PCs are able to sense variations in mechanical properties of the FN deposits and respond to this by changing traction force, cell spreading area, and the size of cell matrix adhesions. Our findings also point to a mechanoresponsive beha-

vior of PCs that significantly differs from that observed for fibroblasts and other cell types. Our findings support a role for FN deposits in the BM as adhesion points for mechanoregulation of the microvasculature by PCs. Our *in vitro* model system of micropillar arrays/micropatterened hydrogels in combination with hiPSC derived-PCs described earlier [32, 65] can be a valuable test-bed to study the mechanisms of PC force regulation in physiology and pathology under well controlled conditions and may serve as a model for drug discovery efforts.

3.5 Apendix

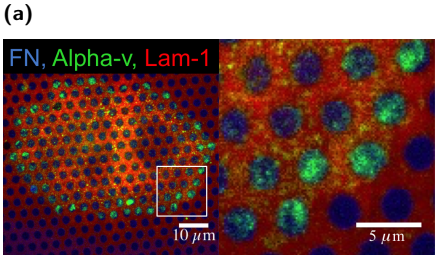

Figure 3.8: PCs (dif31) placed on a pattern of FN and LM-111 depicted in (Fig. 2.2a) with alpha-v integrin labeled (green). Related to Figure 3.1.

3.5 Apendix

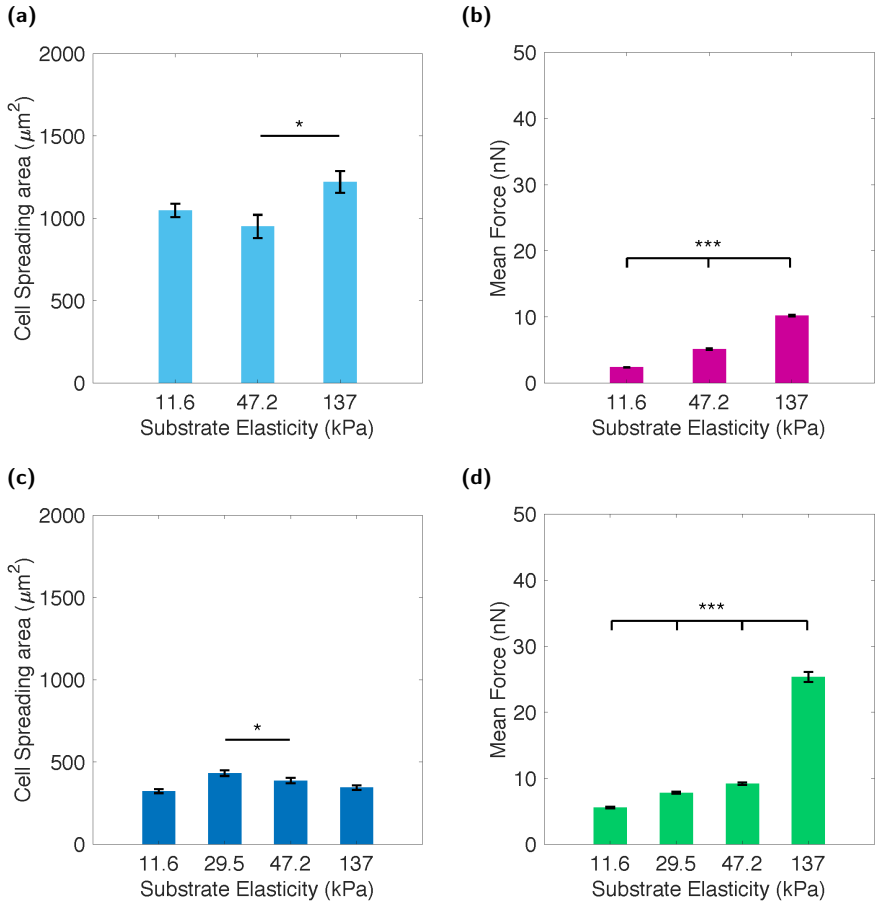

Figure 3.9: SV80 and 3T3 cells average spreading area and force application. (a) SV80 average cell spreading area on PDMS micropillar arrays after 4 hours incubation. (b) SV80 average force application measured after 4 hours incubation. (c) 3T3 average cell spreading area on PDMS micropillar arrays functionalized with FN after 4 hours incubation. (d) 3T3 average force application measured after 4 hours incubation. All error bars are s.e.m. derived from three independent experiments performed in minimum two replicates. At least 30 cells were analyzed from each sample. NS, $P>0.05$; *$P<0.05$; **$P<0.005$; ***$P<0.0005$ according to Mann - Whitney test. Related to Figure 3.3.

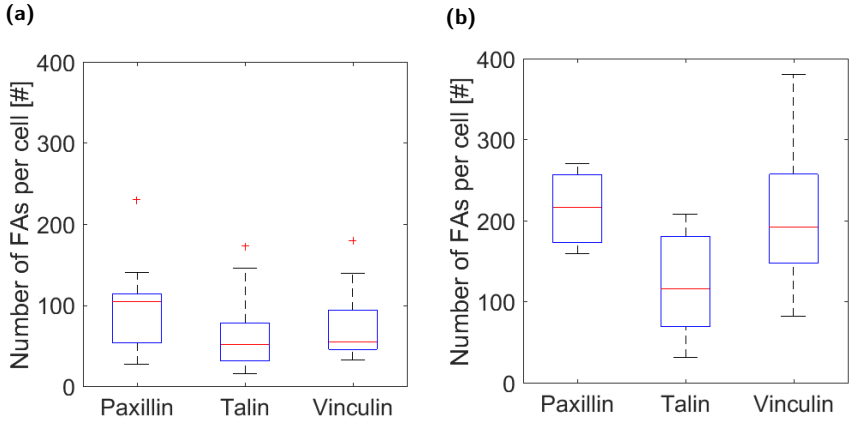

Figure 3.10: (a) Number of FAs per cell for PCs seeded on 137 kPA micropillar arrays stamped with FN. (b) Number of FAs per cell for PCs seeded on 47,2 kPA micropillar array stamped with FN. Results were obtained after 4 hours incubation from three independent experiments performed in minimum two replicates. At least 30 cells were analyzed from each sample. NS, $P>0.05$; *$P<0.05$; **$P<0.005$; ***$P<0.0005$ according to Mann - Whitney test. Related to Figure 3.4.

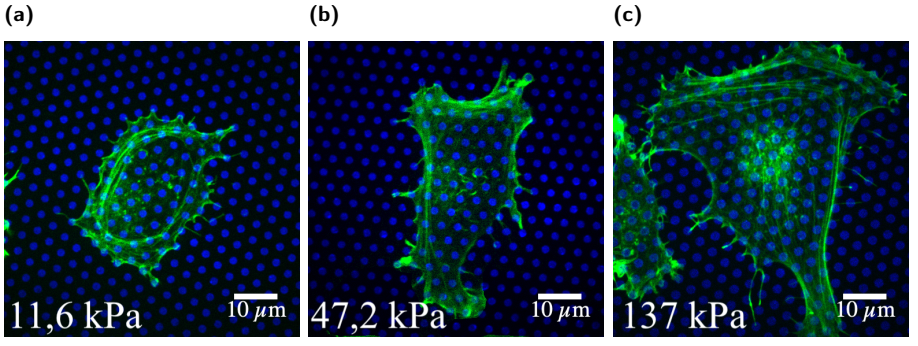

Figure 3.11: Representative images of the actin cytoskeleton organization of SV80 cells (green) seeded on PDMS micropillar arrays of various stiffness stamped with FN (blue): (a) 11,6 kPa, (b) 47,2 kPa, (c) 137 kPa. Related to Figure 3.5.

Bibliography

[1] K.W. Zimmermann. « Der feinere bau der blutcapillares ». In: *Z. Anat. Entwickl.* 68 (1923), pp. 3–109.

[2] Annika Armulik, Guillem Genové and Christer Betsholtz. « Pericytes: developmental, physiological, and pathological perspectives, problems, and promises. » In: *Dev. Cell* 21.2 (2011), pp. 193–215. ISSN: 1534-5807.

[3] Dore-Duffy Paula et al. « CNS microvascular pericytes exhibit multipotential stem cell activity. » In: *J. Cereb. Blood Flow Metab.* 26.5 (2006), pp. 613–24. ISSN: 0271-678X.

[4] Robert D Bell et al. « Pericytes control key neurovascular functions and neuronal phenotype in the adult brain and during brain aging. » In: *Neuron* 68.3 (2010), pp. 409–27. ISSN: 0896-6273.

[5] Annika Armulik et al. « Pericytes regulate the blood-brain barrier. » In: *Nature* 468.7323 (2010), pp. 557–61. ISSN: 0028-0836.

[6] Holger Gerhardt, Hartwig Wolburg and Christoph Redies. « N-cadherin mediates pericytic-endothelial interaction during brain angiogenesis in the chicken ». In: *Dev Dyn* 218.3 (2000), pp. 472–479. ISSN: 1097-0177.

[7] Robert A Hill et al. « Regional Blood Flow in the Normal and Ischemic Brain Is Controlled by Arteriolar Smooth Muscle Cell Contractility and Not by Capillary Pericytes. » In: *Neuron* 87.1 (2015), pp. 95–110. ISSN: 0896-6273.

[8] Anusha Mishra et al. « Astrocytes mediate neurovascular signaling to capillary pericytes but not to arterioles. » In: *Nat. Neurosci.* 19.12 (2016), pp. 1619–1627. ISSN: 1097-6256.

[9] YJ Le Beux and J Willemot. « Actin- and myosin-like filaments in rat brain pericytes. » In: *Anat. Rec.* 190.4 (1978), pp. 811–26. ISSN: 0003-276X.

[10] IH Wallow and B Burnside. « Actin filaments in retinal pericytes and endothelial cells. » In: *Invest. Ophthalmol. Vis. Sci.* 19.12 (1980), pp. 1433–41. ISSN: 0146-0404.

[11] NC Joyce, MF Haire and GE Palade. « Contractile proteins in pericytes. I. Immunoperoxidase localization of tropomyosin. » In: *J. Cell Biol.* 100.5 (1985), pp. 1379–86. ISSN: 0021-9525.

[12] NC Joyce, MF Haire and GE Palade. « Contractile proteins in pericytes. II. Immunocytochemical evidence for the presence of two isomyosins in graded concentrations. » In: *J. Cell Biol.* 100.5 (1985), pp. 1387–95. ISSN: 0021-9525.

[13] Nicola B Hamilton, David Attwell and Catherine N Hall. « Pericyte-mediated regulation of capillary diameter: a component of neurovascular coupling in health and disease ». In: *Frontiers in neuroenergetics* 2 (2010).

[14] Claire M Peppiatt et al. « Bidirectional control of CNS capillary diameter by pericytes. » In: *Nature* 443.7112 (2006), pp. 700–4. ISSN: 0028-0836.

[15] Kassandra Kisler et al. « Pericyte degeneration leads to neurovascular uncoupling and limits oxygen supply to brain ». Czech. In: *Nat Neurosci* 20.3 (2017), pp. 406–416. ISSN: 1097-6256.

[16] Catherine N Hall et al. « Capillary pericytes regulate cerebral blood flow in health and disease. » In: *Nature* 508.7494 (2014), pp. 55–60. ISSN: 0028-0836.

[17] Muge Yemisci et al. « Pericyte contraction induced by oxidative-nitrative stress impairs capillary reflow despite successful opening of an occluded cerebral artery. » In: *Nat. Med.* 15.9 (2009), pp. 1031–7. ISSN: 1078-8956.

[18] Anthony P Hall. « Review of the pericyte during angiogenesis and its role in cancer and diabetic retinopathy. » In: *Toxicol Pathol* 34.6 (2006), pp. 763–75. ISSN: 0192-6233.

[19] Katsukuni Fujimoto. « Pericyte-endothelial gap junctions in developing rat cerebral capillaries: A fine structural study ». In: *Anatomical Rec* 242.4 (1995), pp. 562–565. ISSN: 1097-0185.

[20] Emmanuelle Tillet et al. « N-cadherin deficiency impairs pericyte recruitment, and not endothelial differentiation or sprouting, in embryonic stem cell-derived angiogenesis. » In: 310.2 (2005), pp. 392–400. ISSN: 0014-4827.

[21] Amber N Stratman et al. « Pericyte recruitment during vasculogenic tube assembly stimulates endothelial basement membrane matrix formation. » In: *Blood* 114.24 (2009), pp. 5091–101. ISSN: 0006-4971.

[22] Ombretta Salvucci et al. « EphrinB reverse signaling contributes to endothelial and mural cell assembly into vascular structures ». In: *Blood* 114.8 (2009), pp. 1707–1716. ISSN: 0006-4971.

[23] Ombretta Salvucci and Giovanna Tosato. *Essential Roles of EphB Receptors and EphrinB Ligands in Endothelial Cell Function and Angiogenesis*. Vol. 114. sciencedirect, 2012. ISBN: 9780123865038.

[24] Deana M Ferreri et al. « N-cadherin levels in endothelial cells are regulated by monolayer maturity and p120 availability. » In: 15.4 (2008), pp. 333–49. ISSN: 1541-9061.

[25] H Gerhardt et al. « N-cadherin expression in endothelial cells during early angiogenesis in the eye and brain of the chicken: relation to blood-retina and blood-brain barrier development ». In: *Eur J Neurosci* 11.4 (1999), pp. 1191–1201. ISSN: 1460-9568.

[26] Lema F Yousif, Jacopo Russo and Lydia Sorokin. « Laminin isoforms in endothelial and perivascular basement membranes ». In: 7.1 (2013), p. 101110. ISSN: 1933-6918.

[27] Willi Halfter et al. « The bi-functional organization of human basement membranes. » In: *PLoS ONE* 8.7 (2013), e67660. ISSN: 1932-6203.

[28] PJ Courtoy and J Boyles. « Fibronectin in the microvasculature: localization in the pericyte-endothelial interstitium. » In: *J. Ultrastruct. Res.* 83.3 (1983), pp. 258–73. ISSN: 0022-5320.

[29] Annika Armulik, Alexandra Abramsson and Christer Betsholtz. « Endothelial-pericyte interactions. » In: *Circ. Res.* 97.6 (2005), pp. 512–23. ISSN: 0009-7330.

[30] Ethan A Winkler, Robert D Bell and Berislav V Zlokovic. « Central nervous system pericytes in health and disease ». In: *Nature Neuroscience* 14.11 (2011), pp. 1398–1405. ISSN: 1097-6256.

[31] Valeria V Orlova et al. « Functionality of Endothelial Cells and Pericytes From Human Pluripotent Stem Cells Demonstrated in Cultured Vascular Plexus and Zebrafish Xenografts ». In: *Arteriosclerosis Thrombosis Vasc Biology* 34.1 (2014), pp. 177–186. ISSN: 1079-5642.

[32] Valeria V Orlova et al. « Generation, expansion and functional analysis of endothelial cells and pericytes derived from human pluripotent stem cells. » In: *Nat Protoc* 9.6 (2014), pp. 1514–31. ISSN: 1750-2799.

[33] Hayri Balcioglu et al. « Substrate rigidity modulates the association between traction forces and molecular composition of cell matrix adhesions ». In: *in preparation* ().

[34] Ravi A Desai, Natalia M Rodriguez and Christopher S Chen. « Stamp-off" to micropattern sparse, multicomponent features. » In: *Methods in Cell Biology* 119 (2014), pp. 3–16. ISSN: 0091-679X.

[35] Hedde van Hoorn et al. « The Nanoscale Architecture of Force-Bearing Focal Adhesions ». In: *Nano letters* 14 (2014), pp. 4257–4262.

[36] Olivia du Roure et al. « Force mapping in epithelial cell migration. » In: *Proc. Natl. Acad. Sci. U.S.A.* 102.7 (2005), pp. 2390–5. ISSN: 0027-8424.

[37] Thomas Grevesse et al. « A simple route to functionalize polyacrylamide hydrogels for the independent tuning of mechanotransduction cues. » In: *Lab on a Chip* 13.5 (2013), pp. 777–80. ISSN: 1473-0189.

[38] Xue Jiang et al. « Cell Growth in Response to Mechanical Stiffness is Affected by Neuron- Astroglia Interactions ». In: *The Open Neuroscience Journal* 1.1 (2007), pp. 7–14. ISSN: 1874-0820.

[39] Thomas Grevesse et al. « Opposite rheological properties of neuronal microcompartments predict axonal vulnerability in brain injury ». In: *Scientific Reports* 5 (2015), p. 9475.

[40] John L Tan et al. « Cells lying on a bed of microneedles: an approach to isolate mechanical force. » In: *Proc. Natl. Acad. Sci. U.S.A.* 100.4 (2003), pp. 1484–9. ISSN: 0027-8424.

[41] Jianping Fu et al. « Mechanical regulation of cell function with geometrically modulated elastomeric substrates. » In: *Nat. Methods* 7.9 (2010), pp. 733–6. ISSN: 1548-7091.

[42] HE Balcioglu et al. « The integrin expression profile modulates orientation and dynamics of force transmission at cell-matrix adhesions ». In: *J Cell Sci* 128.7 (2015), pp. 1316–1326. ISSN: 0021-9533.

[43] C. Dambrot et al. « Polycistronic lentivirus induced pluripotent stem cells from skin biopsies after long term storage, blood outgrowth endothelial cells and cells from milk teeth ». In: *Differentiation* 85.3 (2013), pp. 101–109. ISSN: 0301-4681.

[44] Takayuki Okamoto et al. « Gap junction-mediated regulation of endothelial cellular stiffness ». In: *Sci Reports* 7.1 (2017), p. 6134. ISSN: 2045-2322.

[45] Zhongkui Hong et al. « Vascular Smooth Muscle Cell Stiffness and Adhesion to Collagen I Modified by Vasoactive Agonists ». In: *Plos One* 10.3 (2015), e0119533.

[46] Tony Yeung et al. « Effects of substrate stiffness on cell morphology, cytoskeletal structure, and adhesion. » In: *Cell Motil. Cytoskeleton* 60.1 (2005), pp. 24–34. ISSN: 0886-1544.

[47] RJ Pelham and Yl Wang. « Cell locomotion and focal adhesions are regulated by substrate flexibility. » In: *Proc. Natl. Acad. Sci. U.S.A.* 94.25 (1997), pp. 13661–5. ISSN: 0027-8424.

[48] Nathalie Q Balaban et al. « Force and focal adhesion assembly: a close relationship studied using elastic micropatterned substrates ». In: *Nature Cell Biology* 3.5 (2001), pp. 466–472. ISSN: 1465-7392.

[49] Léa Trichet et al. « Evidence of a large-scale mechanosensing mechanism for cellular adaptation to substrate stiffness ». In: *Proc National Acad Sci* 109.18 (2012), pp. 6933–6938. ISSN: 0027-8424.

[50] Colin Grant and Peter Twigg. « Pseudostatic and Dynamic Nanomechanics of the Tunica Adventitia in Elastic Arteries Using Atomic Force Microscopy ». In: *Acs Nano* 7.1 (2013), pp. 456–464. ISSN: 1936-0851.

[51] M Balooch et al. « Viscoelastic properties of demineralized human dentin measured in water with atomic force microscope (AFM)-based indentation. » In: *J. Biomed. Mater. Res.* 40.4 (1998), pp. 539–44. ISSN: 0021-9304.

[52] Ali Hemmasizadeh, Michael Autieri and Kurosh Darvish. « Multilayer material properties of aorta determined from nanoindentation tests. » In: *J Mech Behav Biomed Mater* 15 (2012), pp. 199–207. ISSN: 1878-0180.

[53] Julie C Kohn, Marsha C Lampi and Reinhart-King, Cynthia A. « Age-related vascular stiffening: causes and consequences ». In: *Frontiers In Genetics* 06 (2015). ISSN: 1664-8021.

[54] Xiaoming Zhou et al. « Fibronectin fibrillogenesis regulates three-dimensional neovessel formation ». In: 22.9 (2008), pp. 1231–1243. ISSN: 0890-9369.

[55] S Morikawa et al. « Abnormalities in pericytes on blood vessels and endothelial sprouts in tumors ». In: *The American Journal of Pathology* (2002).

[56] Sophie Dulauroy et al. « Lineage tracing and genetic ablation of ADAM12+ perivascular cells identify a major source of profibrotic cells during acute tissue injury ». In: *Nat Med* 18.8 (2012), p. 1262. ISSN: 1546-170X.

[57] A. Dellavalle et al. « Pericytes resident in postnatal skeletal muscle differentiate into muscle fibres and generate satellite cells ». In: *Nat Commun* 2.1 (2011), p. 499. ISSN: 2041-1723.

[58] Jifan Feng et al. « Dual origin of mesenchymal stem cells contributing to organ growth and repair ». In: *Proc National Acad Sci* 108.16 (2011), pp. 6503–6508. ISSN: 0027-8424.

[59] Elosegui-Artola Alberto, Xavier Trepat and Roca-Cusachs Pere. « Control of Mechanotransduction by Molecular Clutch Dynamics ». In: *Trends Cell Biol* (0). ISSN: 0962-8924.

[60] CE Chan and DJ Odde. « Traction dynamics of filopodia on compliant substrates ». In: *Science* (2008). ISSN: 0036-8075.

[61] BL Bangasser et al. « Shifting the optimal stiffness for cell migration ». In: *Nature* (2017). ISSN: 2041-1723.

[62] Marion Ghibaudo et al. « Traction forces and rigidity sensing regulate cell functions ». In: 4.9 (2008), pp. 1836–1843. ISSN: 1744-683X.

[63] Sangyoon J Han et al. « Decoupling substrate stiffness, spread area, and micropost density: a close spatial relationship between traction forces and focal adhesions. » In: *Biophys. J.* 103.4 (2012), pp. 640–8. ISSN: 0006-3495.

[64] A Elosegui-Artola et al. « Mechanical regulation of a molecular clutch defines force transmission and transduction in response to matrix rigidity ». In: *Nature cell biology* (2016). ISSN: 1465-7392.

[65] Ayelet Dar et al. « Multipotent Vasculogenic Pericytes From Human Pluripotent Stem Cells Promote Recovery of Murine Ischemic Limb ». In: 125.1 (2012), pp. 87–99. ISSN: 0009-7322.

BIBLIOGRAPHY